

Investigation of Step-Skew Rotor on Electromagnetic Force and Vibration in Integral-Slot IPMSM Driven with SVPWM Technique

Zhi Xu¹, Shunqing Xu^{2,*}, Dandan Liu², and Zhishu Yao²

¹*School of Mechanical Engineering UGS College, Yancheng Institute of Technology, Yancheng, China*

²*School of Electrical Engineering, Yancheng Institute of Technology, Yancheng, China*

ABSTRACT: This paper investigates the effects of the step-skew rotor on the electromagnetic vibration performance of a 72-slot/12-pole interior permanent magnet synchronous machine (IPMSM) considering the carrier sideband current harmonics. Firstly, the effect of the step-skew rotor on carrier sideband current harmonics generated by the space vector pulse-width modulation technique is investigated. Second, the interaction electromagnetic field near the first carrier frequency of the 72-slot/12-pole IPMSM is analytically investigated. The effects of the step-skew rotor on the electromagnetic force at low-medium and carrier frequency domain are discussed. The force modulation effect is also considered to investigate the effects of the step-skew rotor on the 72nd-order force and the zeroth mode vibration. Finally, the vibration responses of two IPMSMs — with and without the step-skew rotor — are simulated to validate the suppression effect of this structure on the 72nd-order force. The simulation results demonstrate that the step-skew rotor design effectively reduces vibration acceleration by 75.7% at 12 times of the fundamental frequency and 30.4% at carrier sideband frequency.

1. INTRODUCTION

The electromagnetic vibration performance of the electrical machine in electric vehicles has received much attention in recent years, in which integral-slot interior permanent magnet synchronous machine (IPMSM) is widely used in electrical vehicle applications due to its wide operating speed range [1, 2]. Step-skew rotor design is an effective method to reduce the electromagnetic vibration response of the IPMSM and has been widely used in the IPMSM in electric vehicles. Some researchers focus on the effects of step-skew rotor design on electromagnetic performance and low-medium frequency vibration [3–5]. In addition, step-skew rotor design can reduce cogging torque and torque ripple, and improve the sinusoidal property of back electromotive force [6, 7]. Thus, step-skew rotor design is a commonly used choice for improving the electromagnetic performance and vibration response. However, investigations of electromagnetic force and vibration performance caused by high-frequency sideband carrier harmonics, considering the step-skew rotor design, are insufficient. The high-frequency vibration of the IPMSM will cause unpleasant noise that harms human hearing. Therefore, it is worthy to investigate the effect of the step-skew rotor on the electromagnetic vibration of the IPMSM.

In general, the electromagnetic vibration response of an IPMSM is mainly caused by the electromagnetic force harmonics with non-zero frequency acting on the stator tooth surface. These harmonics are affected by the magnetic flux density from the permanent magnetic (PM) field and armature reaction field. The carrier sideband current harmonics from the drive system with space vector pulse width modulation (SVPWM) technique

will generate abundant armature magnetic field harmonics near the carrier frequency range. These armature magnetic field harmonics near carrier frequency will interact with the permanent magnet field to generate electromagnetic force harmonics near the carrier frequency range. Nowadays, lots of investigation has been applied to the electromagnetic force, vibration, and acoustic noise of electrical machines generated from high-frequency sideband current harmonics. In [8], the spatial and temporal characteristics of the electromagnetic force near the carrier frequency of electrical machines with different slot-pole combinations were compared. However, only the sideband electromagnetic force harmonics near the first carrier frequency range were investigated. The electromagnetic force harmonics near the double and higher times carrier frequency domain were neglected. The detailed analytical investigation of the carrier sideband current harmonics generated by the SVPWM technique was deduced in [9] and [10]. The results showed that the amplitudes of the carrier sideband current harmonics are related to the modulation ratio, inductance in the dq -axis, carrier frequency, and rotational speed.

Lots of researches focus on the high-frequency vibration and noise caused by carrier sideband current harmonics [11–13]. These works prove that studying the vibrations caused by SVPWM (or PWM, SPWM) is meaningful. To suppress the high-frequency sideband vibration of electrical machines, many researchers have proposed improved modulation strategies to suppress or eliminate carrier sideband current harmonics. Random modulation technique is widely used to cause the current harmonics originally near the switching frequency to spread to other frequency ranges [14]. The phase-shift technique of carrier wave was proposed to reduce the carrier sideband current and vibration for a two-segment, three-phase elec-

* Corresponding author: Shunqing Xu (xsq_ycit@126.com).

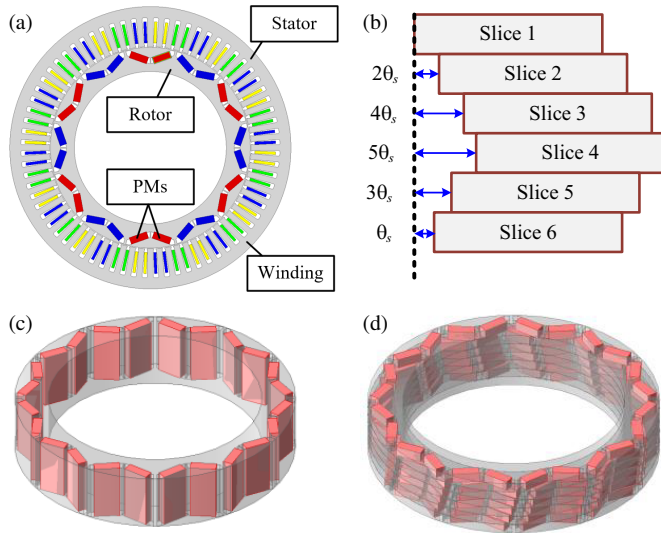


FIGURE 1. 72-slot/12-pole IPMSM. (a) 2-D model. (b) Step-skew rotor core arrangement. (c) Normal rotor. (d) Step-skew rotor.

trical machine [15]. By phase shifting of 1/4 of the switching cycle in the carrier, the carrier current harmonics can be significantly reduced. Nevertheless, much literature has proposed improvements in drive control systems to suppress the carrier current harmonics and vibrations. The effects of stator, rotor, and winding topology on carrier current harmonics and vibration for electrical machines, especially for IPMSM, are insufficient. Therefore, this paper will investigate the effects of step-skew rotor topology on the carrier current harmonics and, hence, vibration response for the integral-slot IPMSM.

The purpose of this paper is extending the traditional research on step-skew rotor by addressing the electromagnetic force harmonics around the carrier frequencies, which have been overlooked in previous studies. The outline of this paper is organized as follows. The outline of this paper is organized as follows. The description of the prototype of two 72-slot/12-pole IPMSMs with and without the V-typed step-skew rotor will be introduced in Section 2. Section 3 will investigate the primary carrier sideband current harmonics of the 72-slot/12-pole IPMSM with the SVPWM technique. The effect of the step-skew rotor on the amplitude of these current harmonics will be introduced by the finite element analysis (FEA) method. In Section 4, the electromagnetic force density of the 72-slot/12-pole IPMSM will be analytically derived. The effects of step-skew rotor design on the electromagnetic force harmonics near the carrier frequency will be discussed. In Section 5, two 72-slot/12-pole IPMSMs will be tested to validate the suppressive effect of V-typed step-skew rotor design on carrier sideband vibration performance. Finally, the conclusion of this paper will be given in Section 6.

2. ELECTROMAGNETIC MODEL OF 72-SLOT/12-POLE IPMSM

Two three-phase 72-slot/12-pole IPMSMs are designed for this investigation without and with step-skewed rotor. It should be noticed that these two IPMSMs have the same 2-D model but

TABLE 1. Parameters of two 72-slot/12-pole IPMSMs.

Items (unit)	Value	
Rotor type	Normal	Step-skew
Stator outer diameter (mm)	370	
Stator inner diameter (mm)	265	
Core stack length (mm)	55	
Air-gap length (mm)	1	
Tooth width (mm)	7.4	
Number of turns per slot	27	
PM material	N42UH	
PM length/width (mm)	24/9	
Rib width (mm)	3	
Rotor axial segments	1	6
Skew angle (deg)	0	2, 3, 4, 5, 1
D-axis inductance (mH)	4.4	4.87
Q-axis inductance (mH)	8.7	8.55
Flux linkage (Wb)	0.1739	0.1713
DC link voltage (V)	400	
Switch frequency (Hz)	10000	

different rotor topologies. Fig. 1 shows the 2-D model and step-skew rotor of the 72-slot/12-pole IPMSM. The skew angle θ_s is 1 deg, and the rotor segments are six of the IPMSM with the step-skew rotor. Table 1 summarizes the detailed parameters of these two IPMSMs.

3. EFFECTS OF STEP-SKEW ROTOR TOPOLOGY ON CARRIER CURRENT HARMONICS

3.1. Carrier Sideband Voltage Harmonics in Inverter

As for SVPWM technique, the carrier sideband current harmonics in IPMSM are caused by the output carrier sideband voltage from the inverter. Applying the double Fourier expansion for output carrier sideband voltage, the output carrier sideband voltage of phase A close to the carrier frequency of the inverter can be obtained through [9] and [10]. The sideband voltage in (1) should first be transferred into the dq -axis using the transfer matrix to obtain the carrier sideband current harmonics. Then, the sideband current harmonics in the dq -axis can be approximately expressed based on the vector relationship between voltage and current in IPMSM as follows:

$$\begin{cases} i_{d-\omega_\mu} = \frac{u_{d\mu}}{j\omega_\mu L_d} \\ i_{q-\omega_\mu} = \frac{u_{q\mu}}{j\omega_\mu L_q} \end{cases} \quad (1)$$

where ω_μ is the angular frequency of the sideband current and voltage harmonics, and L_d and L_q represent the inductances of the d -axis and q -axis, respectively. This paper only investigates the carrier sideband current harmonics close to the first carrier frequency (10 kHz). Therefore, the carrier sideband current harmonics in phase winding can be obtained through the inverse transformation from dq -axis. Fig. 2 shows the simulated three-phase current waveforms and their fast Fourier transform (FFT)

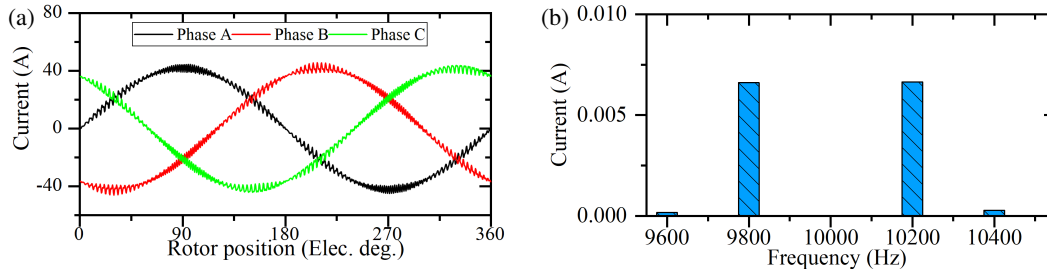


FIGURE 2. Current waveform involving carrier sideband current harmonics at 1000 r/min. (a) Phase current. (b) Current FFT results of phase A in carrier frequency domain.

components of the 72-slot/12-pole IPMSM under 1000 r/min. The results show that the primary current harmonics near the first carrier frequency include $f_s \pm 2f_e$ and $f_s \pm 4f_e$, where $f_s = 10$ kHz and $f_e = 100$ Hz are carrier frequency and fundamental electrical frequency, respectively.

3.2. Effects of Step-Skew Rotor on Carrier Sideband Current

From the above analytical expression, the amplitude of the carrier sideband current is mainly determined by the DC-link voltage of the IPMSM drive system, modulation coefficient, and dq -axis inductance. Fig. 3 compares the simulated phase current waveforms and spectral analysis of the 72-slot/12-pole IPMSM with and without step-skew rotor in no-load condition at 1000 r/min, respectively. The FFT results show that the amplitudes of carrier sideband current harmonics of two IPMSMs are almost equal due to the tiny difference in modulation ratio and inductance in the dq -axis between two IPMSMs.

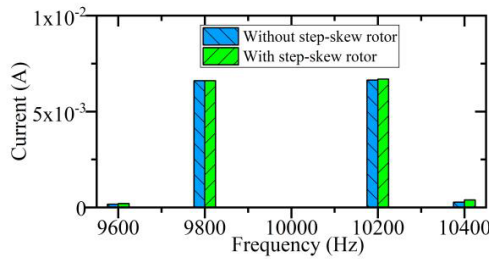


FIGURE 3. Comparison of phase current FFT results of two IPMSMs close to carrier frequency.

4. EFFECTS OF STEP-SKEW ROTOR TOPOLOGY ON CARRIER SIDEBAND ELECTROMAGNETIC FORCE

The radial electromagnetic force acting on stator teeth is the primary vibration source of the IPMSMs. The Maxwell stress tensor method can calculate the radial electromagnetic force density based on the radial and tangential components of air-gap flux density. As a result, the radial and tangential electromagnetic force densities in the air-gap can be approximated as:

$$\begin{cases} P_{rad}(\theta, t) = \frac{B_{rad}^2(\theta, t) - B_{tan}^2(\theta, t)}{2\mu_0} \\ P_{tan}(\theta, t) = \frac{B_{rad}(\theta, t)B_{tan}(\theta, t)}{\mu_0} \end{cases} \quad (2)$$

where μ_0 is the vacuum permeability; θ is the mechanical angle; t represents time; B_{rad} and B_{tan} are radial and tangential magnetic flux densities in air gap, respectively. The carrier sideband electromagnetic vibration is mainly influenced by the interaction field of the PM magnetic field and carrier sideband armature reaction field. Therefore, the effects of step-skew rotor design on the interaction of magnetic field and electromagnetic force will be investigated as follows.

4.1. Analytical of Carrier Sideband Electromagnetic Field Harmonics

The tangential electromagnetic force and magnetic flux density can be neglected due to their tiny amplitude compared with the radial components. Therefore, B_{rad} can be expressed as:

$$B_{rad}(\theta, t) = [B_{PM}(\theta, t) + B_{Arm}(\theta, t)] \Lambda_a \quad (3)$$

where

$$B_{PM}(\theta, t) = \sum_k B_{PM}^k \cos(kp\theta - k\omega_e t) \quad (4)$$

$$B_{arm}(\theta, t) = \sum_{\mu} \sum_v B_{arm-\mu v} \cos(vN_t\theta - \omega_{\mu}t - \varphi_{\mu}) \quad (5)$$

$$\Lambda_a = \Lambda_s(\theta) \cdot \Lambda_r(\theta, t)$$

$$= \left[\Lambda_{s0} + \sum_{m=1}^{\infty} \Lambda_{sm} \cos(mQ_s\theta) \right]$$

$$\cdot \left[\Lambda_{r0} + \sum_{n=1}^{\infty} \Lambda_{rn} \cos(np\theta - n\omega_e t) \right]$$

$$= \Lambda_0 + \sum_{m=1}^{\infty} \Lambda_{r0} \Lambda_{sm} \cos(mQ_s\theta)$$

$$+ \sum_{k_r=1}^{\infty} \Lambda_{s0} \Lambda_{rn} \cos(np\theta - n\omega_e t)$$

$$+ \frac{1}{2} \sum_{m=1}^{\infty} \sum_{n=1}^{\infty} \Lambda_{sm} \Lambda_{rn}$$

$$\cos[(mQ_s \mp np)\theta \pm n\omega_e t] \quad (6)$$

where B_{PM} and B_{arm} are permanent magnetic field and armature reaction field magnetomotive force, respectively; N_t =

$GCD(72, 6) = 6$, ω_μ and φ_μ are the frequency and phase angle of the μ th order current harmonic, respectively; Λ_a is the air-gap permeability function of the IPMSM; Q_s is the number of stator slot; $\Lambda_s(\theta)$ and $\Lambda_r(\theta, t)$ are permeability function of stator and rotor of IPMSM. The magnetic field phase angle of each rotor segment will be changed due to the step-skew rotor design. The radial PM flux density can be treated as synthesis by each rotor segment as:

$$B_{PM}(\theta, t) = \sum_{\varepsilon} \sum_k \frac{1}{\varepsilon} B_{PM-eq}^k \cos \left\{ k [\theta - \gamma (\varepsilon - 1)] p - k \omega_e t \right\} \quad (7)$$

where ε represents the number of rotor segments ($\varepsilon = 6$ in this paper), and γ is the skew angle of each rotor segment. Fig. 4 shows the comparison of B_r of two IPMSMs, and B_r in the IPMSMs with step-skew rotor is synthesized from each segmented rotor. It can be seen that the step-skew rotor design causes the reduction of synthetic magnetic field density harmonics due to the phase shift effect, especially for 18th-, 30th-, and 42nd-order components.

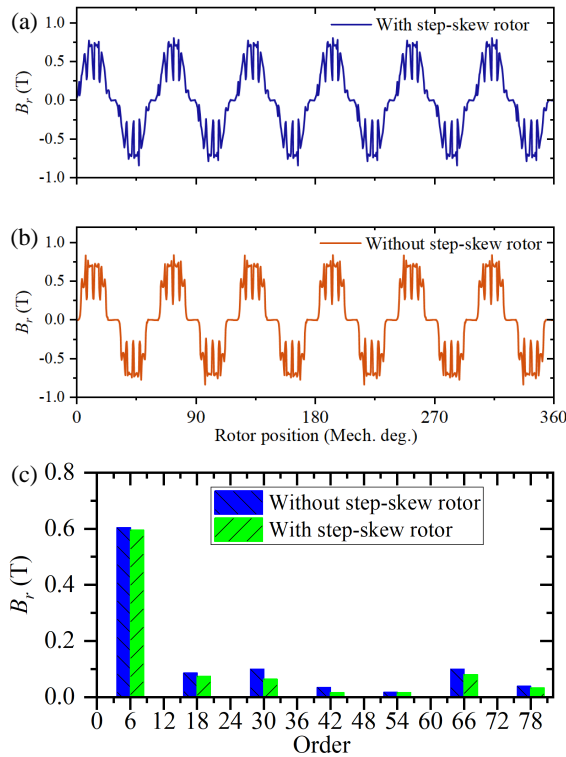


FIGURE 4. Comparison of B_r of two IPMSMs. (a) Waveform. (b) FFT results.

4.2. Analytical of Carrier Sideband Electromagnetic Force Harmonics

Since the harmonic amplitudes of the stator and rotor permeance are very small, they are neglected here for simplifying the analysis. The radial electromagnetic force density from each rotor segment can be expressed by combining (4)–(8):

$$P_{rad}(\theta, t) \approx \sum_{\varepsilon} \sum_{\mu} \sum_k \sum_v \frac{P_{rad-\mu kv}}{\varepsilon}$$

$$\cos \left\{ \begin{array}{l} kp [\theta - \gamma (\varepsilon - 1)] \\ \pm v N_t \theta \\ \pm (\omega_\mu \pm k \omega_e) t \pm \varphi_\mu \end{array} \right\} \quad (8)$$

According to (8), abundant radial electromagnetic force density components will be near the carrier frequency. The main spatial order of the radial carrier sideband electromagnetic forces can be 0th-, 12th-, 24th-, 36th-, 48th-, 60th-, and 72nd-order for 72-slot/12-pole IPMSM. Besides that, the phase of electromagnetic force density from different rotor segments will be different due to the step-skew rotor. These force components will generate different vibration modes of the IPMSM. The vibration displacement amplitude of each mode can be expressed as:

$$\left\{ \begin{array}{l} D_{order=0} = \frac{R_y R_s P_{order=0}}{E T_y} \\ D_{order \geq 2} = \frac{12 R_y^3 R_s P_{order \geq 2}}{E T_y^3 (order^2 - 1)^2} \\ \frac{D_{order=0}}{D_{order \geq 2}} = \frac{(order^2 - 1)^2}{12} \left(\frac{T_y}{R_y} \right)^2 \frac{P_{order=0}}{P_{order \geq 2}} \end{array} \right. \quad (9)$$

where R_y and T_y are the average radius and radial thickness of the stator yoke, respectively; E is the Young's modulus; R_s is the inner radius of the stator, as shown in Fig. 5. It can be seen that the vibration displacement of the stator is inversely proportional to the fourth power of the electromagnetic force order, which is more than two. In addition, the higher the spatial order of the electromagnetic force density is, the higher the ratio $D_{order=0}/D_{order \geq 2}$ is. It means that the zeroth mode vibration displacement is more significant than nonzero order vibration displacement caused by higher order force. Hence, the electromagnetic force density that will cause the zeroth order vibration displacement should be treated as the dominant component to be investigated. According to (8), when $kp \pm v N_t = u Q_s$, the caused vibration mode can be zero. Based on the Nyquist-Shannon sampling process, when the order of the electromagnetic force exceeds half the number of slots, an aliasing effect of the electromagnetic force occurs, also known as the electromagnetic force modulation effect [16].

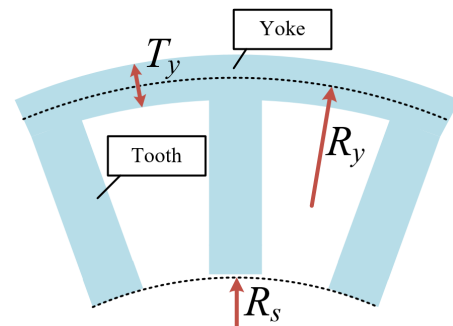


FIGURE 5. Parameters in stator core.

Hence, the 72nd-order radial carrier sideband electromagnetic force is investigated in this paper. The main magnetic field components include the N_t th-, $11N_t$ th-, and $13N_t$ th-order sideband armature reaction field, and the p th-, $11p$ th-, and $13p$ th-order PM field components are considered. Therefore, the radial carrier sideband electromagnetic force components

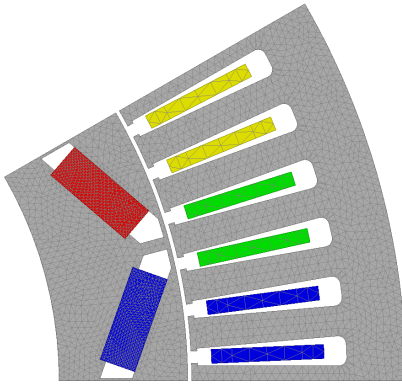


FIGURE 6. Mesh arrangement of 72-slot/12-pole IPMSM for simulation.

caused by $(f_s \pm 2f_e)$ - and $(f_s \pm 4f_e)$ -order carrier sideband current components are listed in Table 2 with their spatial and frequency characteristics.

From Table 2, the step-skew rotor design will reduce the amplitude of the carrier sideband electromagnetic forces due to the radial PM magnetic field reduction. The FEA method is adopted for two IPMSMs to validate the analytical model of carrier sideband electromagnetic force components. Fig. 6 shows the mesh arrangement of the 72-slot/12-pole IPMSM. The rotation speed of the two IPMSMs are both 1000 r/min, which means that the fundamental frequency is 100 Hz. As for the current excitation, the amplitude is 30 A, and advanced phase angle is 45 deg. Based on the vector superposition principle, the electromagnetic forces generated by six segmented rotors can be synthesized into a single concentrated force, as shown in Fig. 7. The electromagnetic force waveforms of two IPMSMs are shown in Fig. 8.

The comparison of 2-D FFT results for the electromagnetic forces of two IPMSMs, analyzed at 0–1200 Hz and in the first carrier frequency range using FEA, is shown in Fig. 9 and Fig. 10, respectively. It can be seen that the (72nd, 1200 Hz)-order radial force density is reduced from 8311.29 N/cm² to

TABLE 2. Origins of 72nd-order carrier sideband electromagnetic forces.

Frequency of current	Spatial order	Frequency of electromagnetic force
$f_s \pm 2f_e$	$p + 11N_t$	$f_s \pm f_e, f_s \pm 3f_e$
	$-p - 11N_t$	$f_s \pm f_e, f_s \pm 3f_e$
	$p - 13N_t$	$f_s \pm f_e, f_s \pm 3f_e$
	$11p + N_t$	$f_s \pm f_e, f_s \pm 3f_e$
	$-11p - N_t$	$f_s \pm f_e, f_s \pm 3f_e$
	$13p - N_t$	$f_s \pm f_e, f_s \pm 3f_e$
$f_s \pm 4f_e$	$p + 11N_t$	$f_s \pm 3f_e, f_s \pm 5f_e$
	$-p - 11N_t$	$f_s \pm 3f_e, f_s \pm 5f_e$
	$p - 13N_t$	$f_s \pm 3f_e, f_s \pm 5f_e$
	$11p + N_t$	$f_s \pm 3f_e, f_s \pm 5f_e$
	$-11p - N_t$	$f_s \pm 3f_e, f_s \pm 5f_e$
	$13p - N_t$	$f_s \pm 3f_e, f_s \pm 5f_e$

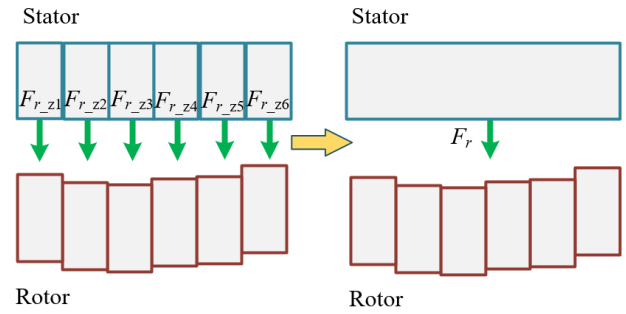


FIGURE 7. Force superposition of electromagnetic force.

2084.45 N/cm². That is because the segmented skew pole design of the rotor suppresses the amplitudes of the p th- and $11p$ th-order PM flux density harmonics, thereby also suppressing the amplitude of the 72nd-order electromagnetic force. In the carrier frequency domain, the (72nd, 10100 Hz)-, (12th, 10300 Hz)-, and $(-72nd, 10100 Hz)$ -order carrier sideband force density components are all reduced. The reason for this phenomenon is consistent with the reason that the (72nd, 1200 Hz)-order radial force is suppressed. However, the amplitudes of $(\pm 72nd, 9700 Hz)$ -order components have increased by more than 1.6% and 0.3%. This is mainly because the amplitude of the 9600 Hz $(f_s - 4f_e)$ current harmonic in the IPMSM with step-skew rotor slightly higher than that in the IPMSM without step-skew rotor, as shown in Fig. 3.

5. VERIFICATION

To verify the above analytical investigation, the vibration acceleration near the first carrier frequency of two IPMSMs should be deduced using the FEA method.

5.1. Modal Parameters

Figure 11 shows the structure model of the 72-slot/12-pole IPMSM, which includes the stator core and aluminum housing. The equivalent material parameters of the housing and stator core considering material anisotropy are given in Table 3. The modal frequencies and modal shape of the 72-slot/12-pole IPMSM are listed in Table 4.

5.2. Vibration Response Simulation

Figure 12 shows the flowchart of the vibration acceleration simulation method. It contains radial electromagnetic force calculation in 2-D FEA, modal simulation, force mapping, and vibration response simulation. The modal superposition method is adopted to calculate the vibration responses.

The radial and tangential electromagnetic force densities in the air gap from the EFA method only approximate all the Maxwell force on the tooth surface. The concentrated radial force on the stator tooth surface are required for the vibration computation. Fig. 13 shows the force transfer process from node force density to concentrated force by using (10).

$$F_{r,Z}^n = L_a R_s \int_{\theta_z - \Delta\theta/2}^{\theta_z + \Delta\theta/2} P_{rad} \cos(\theta_z - \theta) d\theta \quad (10)$$

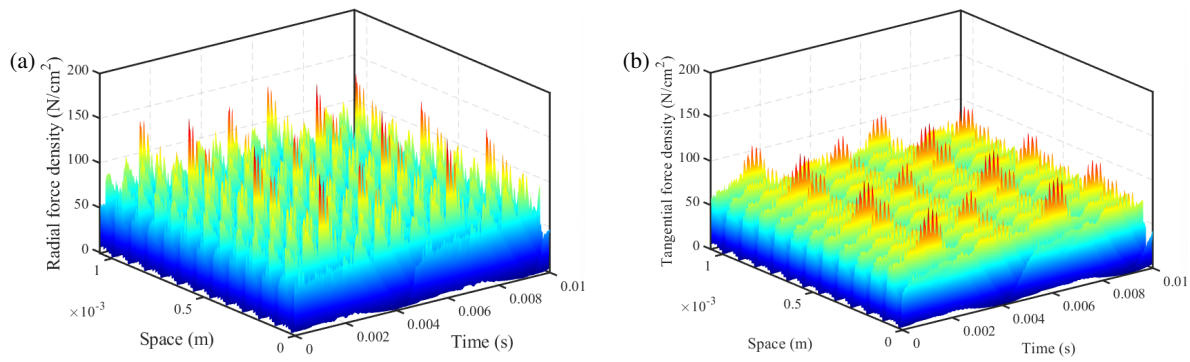


FIGURE 8. Radial electromagnetic force density waveforms of two 72-slot/12-pole IPMSMs. (a) Without step-skew rotor. (b) With step-skew rotor.

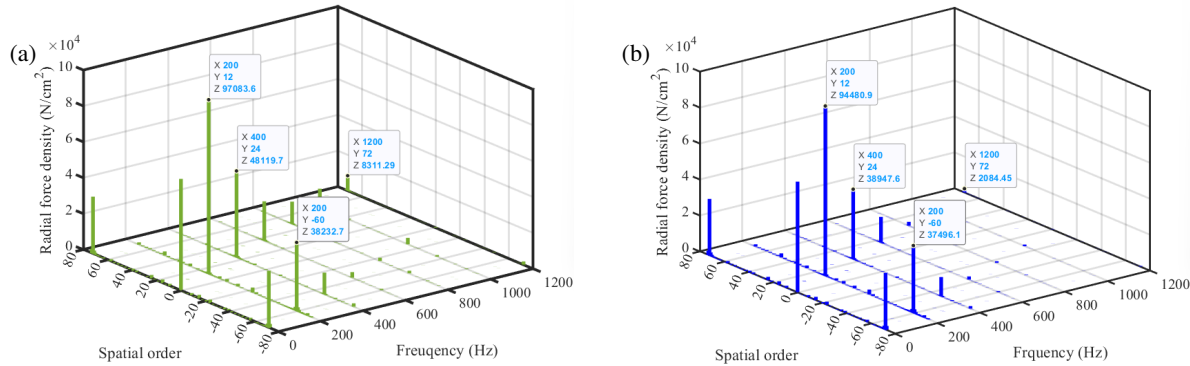


FIGURE 9. 2-D FFT results comparison of radial electromagnetic force density at 0–1200 Hz. (a) Without step-skew rotor. (b) With step-skew rotor.

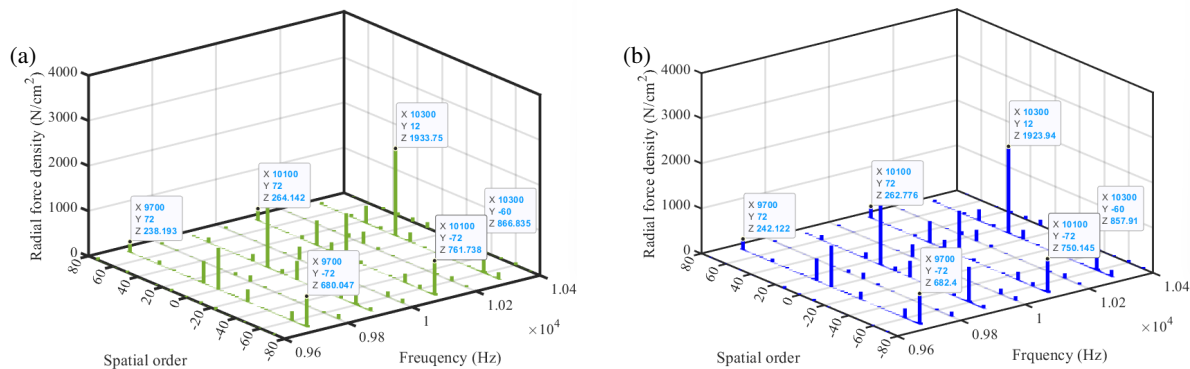


FIGURE 10. 2-D FFT results comparison of radial carrier sideband electromagnetic force density. (a) Without step-skew rotor. (b) With step-skew rotor.

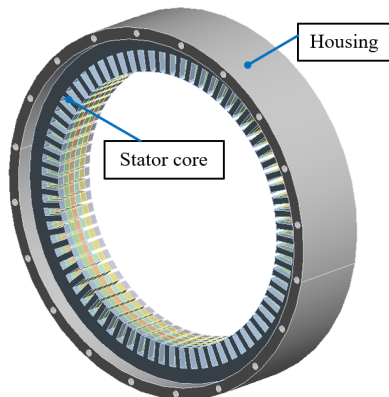


FIGURE 11. Structure model of the 72-slot/12-pole IPMSM.


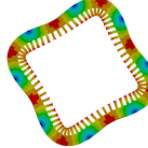
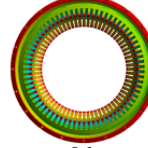
where L_a is the axial length of the stator.

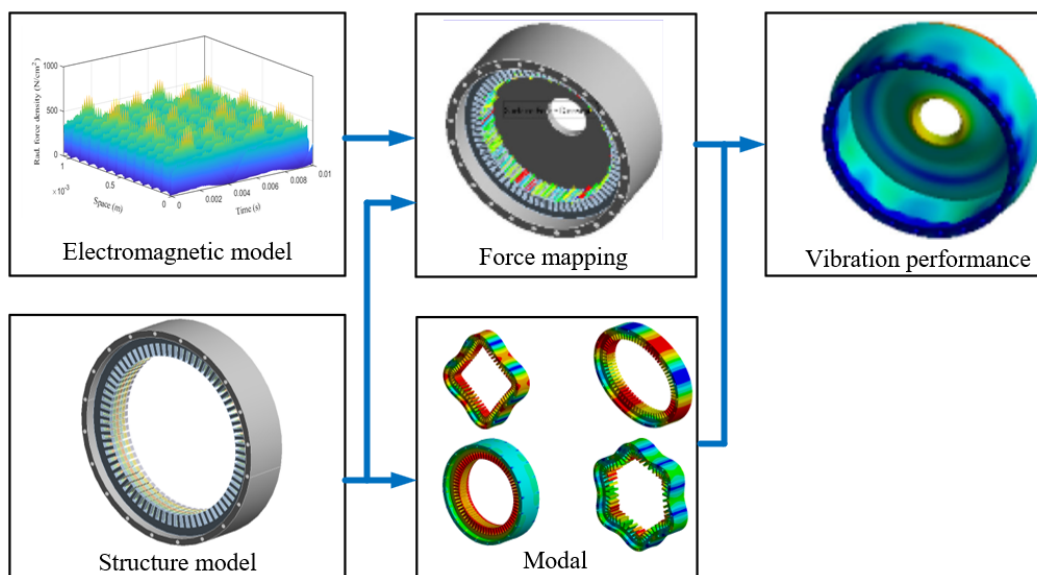
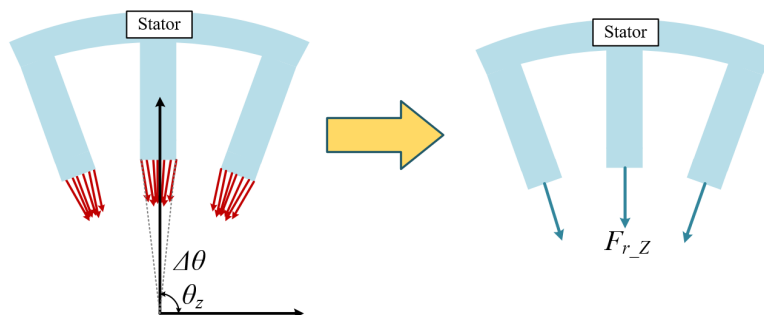
By submitting the simulated force density in Fig. 9 and Fig. 10 to (10), the radial concentrated force can be obtained. Fig. 14 and Fig. 15 show the transferred concentrated force at 0–1200 Hz and carrier frequency domain, respectively. Based on the force modulation effect [16], the 72nd-order distributed force is modulated to zeroth-order concentrated force. The FFT results show that the (0th, 1200 Hz)-order concentrated force is reduced from 13.97 N to 2.68 N by using the step-skew rotor. As for the carrier sideband electromagnetic concentrated force, the zeroth-order components with 9900 Hz ($f_s - f_e$), 10100 Hz ($f_s + f_e$), and 10300 Hz ($f_s + 3f_e$) are all reduced through using the step-skew rotor. The (0th, 9700 Hz)-carrier sideband electromagnetic concentrated force is increased a litter.

TABLE 3. Material parameters.

Part	Density (kg/m ³)	Poisson's ratio	Young's Modulus (GPa)	Shear Modulus (GPa)
Stator core	7860	$u_{xy} = 0.3$ $u_{xz} = u_{yz} = 0.27$	$E_x = E_y = 205$ $E_z = 170$	$G_{yz} = G_{zx} = 26.5$ $G_{xy} = 55$
Housing	2770	0.33	70	25.6

TABLE 4. Modal parameters of 72-slot/12-pole IPMSM.

Modal shape			
	2nd	4th	0th
Simulated	489 Hz	2208 Hz	3489 Hz

**FIGURE 12.** Electromagnetic vibration simulation process.**FIGURE 13.** Illustration of concentrated force transformation.

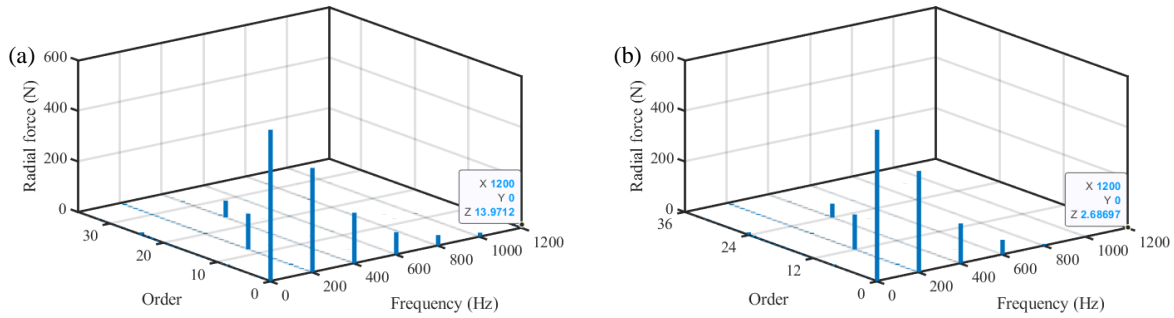


FIGURE 14. FFT results of radial concentrated force of two IPMSMs at 0–1200 Hz. (a) Without step-skew rotor. (b) With step-skew rotor.

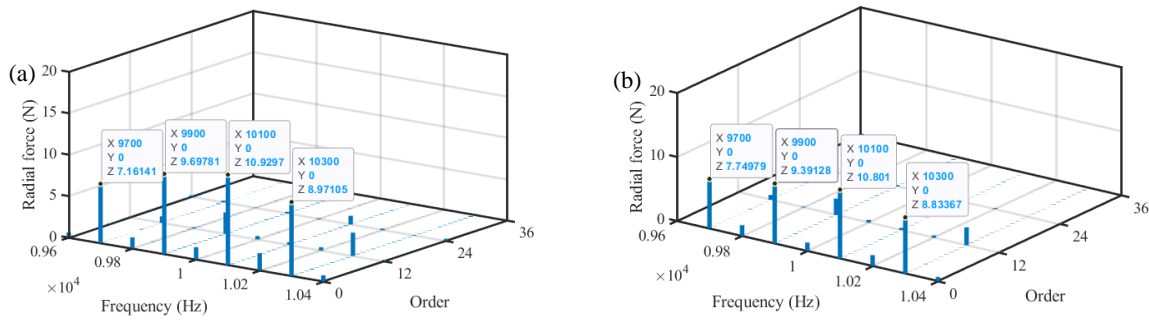


FIGURE 15. FFT results of radial concentrated force of two IPMSMs close to carrier frequency. (a) Without step-skew rotor. (b) With step-skew rotor.

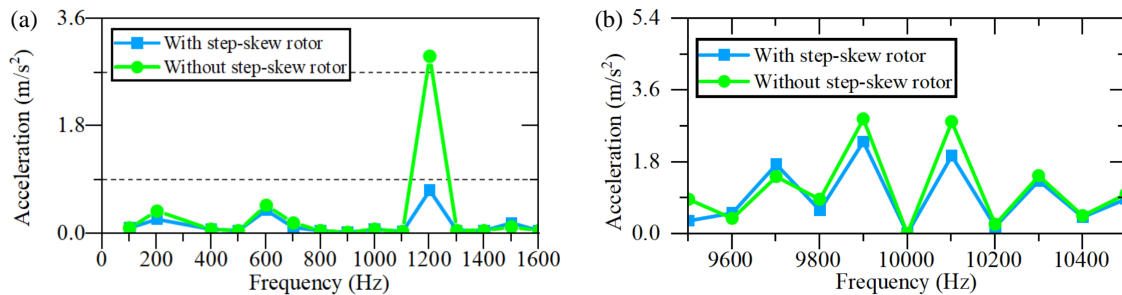


FIGURE 16. Comparison of 72-slot/12-pole IPMSM vibration acceleration at on-load with 1000 r/min. (a) 0–1600 Hz. (b) 9600–10400 Hz.

Figures 16(a) and 16(b) show the simulated vibration acceleration of two 72-slot/12-pole IPMSMs with 1000 r/min at 0–1200 Hz and close to the carrier frequency, respectively. It is clear that the vibration acceleration at 1200 Hz is greatly reduced because the (0th, 1200 Hz)-order concentrated force is suppressed. As for the vibration acceleration close to the carrier frequency, the primary vibration accelerations occur at $f_c \pm f_e$ and $f_c \pm 3f_e$. The vibration accelerations at 9900 Hz ($f_s - f_e$), 10100 Hz ($f_s + f_e$), and 10300 Hz ($f_s + 3f_e$) are all suppressed by using the step-skew rotor. However, the vibration accelerations at 9700 Hz ($f_s - 3f_e$) is increased due to the increase of the (0th, 9700 Hz)-order concentrated force. It indicates that the vibration acceleration close to the first carrier frequency of the IPMSM with a step-skew rotor is smaller than that of the IPMSM without a step-skew rotor in $f_s \pm f_e$ and $f_s + 3f_e$. The step-skew rotor design in this paper can greatly reduce the zeroth mode vibration at $12f_e$ frequency.

6. CONCLUSION

This paper investigates the effects of step-skew rotor design on the carrier sideband current harmonics, carrier sideband electromagnetic force, and vibration acceleration of a 72-slot/12-pole IPMSM. The mechanism of the carrier sideband voltage and current harmonics of six-phase IPMSM with the SVPWM technique has been established. The simulation results show that the step-skew rotor barely affects the amplitude of carrier sideband current harmonics. The effects of the step-skew rotor on the 72nd-order carrier sideband electromagnetic force have been investigated. The simulation results show that the step-skew rotor design can reduce the carrier sideband electromagnetic force due to its phase shift characteristics having a reduced effect on the PM magnetic field. The multi-physic vibration simulations of two IPMSMs have been applied to verify the theoretical analysis. The results show that the step-skew rotor design of integral-slot IPMSM has a suppression effect on

carrier sideband vibration performance. The purpose of this investigation is to provide an analytical method for investigating the effects of step-skew rotor on electromagnetic forces and vibration responses at both low-medium and carrier frequency.

REFERENCES

- [1] Liang, J., D. Liu, Y. Gao, H. Yuan, and X. Liu, "Design and analysis of a novel mechanical variable flux interior permanent magnet synchronous motor," *Progress In Electromagnetics Research C*, Vol. 123, 167–179, 2022.
- [2] Wen, D., X. Zhu, Z. Cheng, Y. Zhang, and W. Zhang, "Sensorless control of interior permanent magnet synchronous motor with triangular transform current self-demodulation in the estimating d - q axis," *Progress In Electromagnetics Research B*, Vol. 103, 75–99, 2023.
- [3] Won, Y.-J., J.-H. Kim, S.-H. Park, J.-H. Lee, S.-M. An, D.-Y. Kim, and M.-S. Lim, "Transfer learning-based design method for cogging torque reduction in PMSM with step-skew considering 3-D leakage flux," *IEEE Transactions on Magnetics*, Vol. 59, No. 11, 1–5, Nov. 2023.
- [4] Peng, C., D. Wang, B. Wang, J. Li, C. Wang, and X. Wang, "Different rotor segmented approaches for electromagnetic vibration and acoustic noise mitigation in permanent magnet drive motor: A comparative study," *IEEE Transactions on Industrial Electronics*, Vol. 71, No. 2, 1223–1233, Feb. 2024.
- [5] Wang, B., D. Wang, X. Wang, C. Wang, and X. Wang, "Design, analysis and testing of a permanent magnet motor with segmented rotor for reducing electromagnetic vibration," in *2023 26th International Conference on Electrical Machines and Systems (ICEMS)*, 5307–5311, Zhuhai, China, 2023.
- [6] Ge, X., Z. Q. Zhu, G. Kemp, D. Moule, and C. Williams, "Optimal step-skew methods for cogging torque reduction accounting for three-dimensional effect of interior permanent magnet machines," *IEEE Transactions on Energy Conversion*, Vol. 32, No. 1, 222–232, Mar. 2017.
- [7] Zhao, W., T. A. Lipo, and B.-I. Kwon, "Torque pulsation minimization in spoke-type interior permanent magnet motors with skewing and sinusoidal permanent magnet configurations," *IEEE Transactions on Magnetics*, Vol. 51, No. 11, 1–4, Nov. 2015.
- [8] Deng, W. and S. Zuo, "Comparative study of sideband electromagnetic force in internal and external rotor PMSMs with SVPWM technique," *IEEE Transactions on Industrial Electronics*, Vol. 66, No. 2, 956–966, Feb. 2019.
- [9] Liang, W., J. Wang, P. C.-K. Luk, W. Fang, and W. Fei, "Analytical modeling of current harmonic components in PMSM drive with voltage-source inverter by SVPWM technique," *IEEE Transactions on Energy Conversion*, Vol. 29, No. 3, 673–680, Sep. 2014.
- [10] Liang, W., W. Fei, and P. C.-K. Luk, "An improved sideband current harmonic model of interior PMSM drive by considering magnetic saturation and cross-coupling effects," *IEEE Transactions on Industrial Electronics*, Vol. 63, No. 7, 4097–4104, Jul. 2016.
- [11] Tsoumas, I. P. and H. Tischmacher, "Influence of the inverter's modulation technique on the audible noise of electric motors," *IEEE Transactions on Industry Applications*, Vol. 50, No. 1, 269–278, Jan.–Feb. 2014.
- [12] Lu, Y., J. Li, and K. Yang, "Study on winding design of dual three-phase electrical machines for circulating current harmonics and vibration suppression," *IEEE Transactions on Industrial Electronics*, Vol. 71, No. 5, 5063–5072, May 2024.
- [13] Lu, Y., J. Li, and K. Yang, "A hybrid calculation method of electromagnetic vibration for electrical machines considering high-frequency current harmonics," *IEEE Transactions on Industrial Electronics*, Vol. 69, No. 10, 10 385–10 395, Oct. 2022.
- [14] Peyghambari, A., A. Dastfan, and A. Ahmadyfard, "Selective voltage noise cancellation in three-phase inverter using random SVPWM," *IEEE Transactions on Power Electronics*, Vol. 31, No. 6, 4604–4610, Jun. 2016.
- [15] Han, X., D. Jiang, T. Zou, R. Qu, and K. Yang, "Two-segment three-phase PMSM drive with carrier phase-shift PWM for torque ripple and vibration reduction," *IEEE Transactions on Power Electronics*, Vol. 34, No. 1, 588–599, Jan. 2019.
- [16] Fang, H., D. Li, R. Qu, and P. Yan, "Modulation effect of slot-structure on vibration response in electrical machines," *IEEE Transactions on Industrial Electronics*, Vol. 66, No. 4, 2998–3007, Apr. 2019.